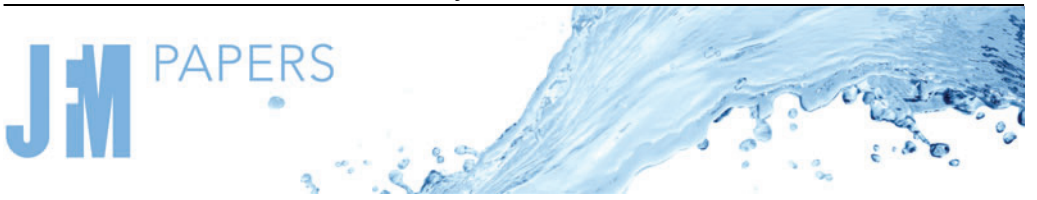
*J. Fluid Mech.* (2025), *vol*. 1003, A7, doi:10.1017/jfm.2024.1195




# Energy thickness in turbulent boundary layer flows

**Tie Wei**[1],†, **Tobias Knopp**[2] **and Zhaorui Li**[3]

[1]Department of Mechanical Engineering, New Mexico Institute of Mining and Technology, 801 Leroy PL, Socorro, NM 87801, USA

[2]Institute of Aerodynamics and Flow Technology, DLR (German Aerospace Center), Bunsenstr. 10, 37073 Gottingen, Germany

[3]Department of Engineering, Texas A&M University-Corpus Christi, 6300 Ocean Drive, Corpus Christi, TX 78412, USA

(Received 2 July 2024; revised 23 October 2024; accepted 8 December 2024)

In this study, we investigate the properties of energy thickness $\delta_3$ in turbulent boundary layer (TBL) flows, a parameter derived solely from the mean streamwise velocity ($U$) profile. Through an analysis of the energy integral equation for zero pressure gradient TBLs, we establish a close relationship between turbulent kinetic energy (TKE) production and $\delta_3$, offering a practical method to estimate TKE production, which is particularly useful in physical experiments where direct measurements are challenging. The significance of $\delta_3$ becomes even more pronounced in TBLs under pressure gradient. Through extensive analysis of numerical and experimental data, we show that the ratio between $\delta_3$ and the momentum thickness $\delta_2$ is a promising criterion for predicting flow separation. Moreover, we derive a new energy integral equation for TBLs under arbitrary pressure gradients, and provide approximations for TKE productions terms by $R_{uv}\,\partial U/\partial y$ and $R_{uu}\,\partial U/\partial x$, and dissipation term by the mean shear. Here, $x$, $y$ represent the streamwise and wall-normal directions, respectively, and $R_{uu}$ and $R_{uv}$ are the Reynolds normal and shear stresses. The accuracy and robustness of the new energy integral equation and the approximation equations are validated using direct numerical simulations data. Our results show that the TKE production by $R_{uv}\,\partial U/\partial y$ and the overall productions consistently remain positive, reflecting a continuous conversion of mean kinetic energy into TKE across all TBLs. However, under strong favourable pressure gradients, TKE production by $R_{uu}\,\partial U/\partial x$ becomes negative, indicating a reverse energy transfer from TKE to mean kinetic energy.

**Key words:** boundary layer separation, turbulent boundary layers

† Email address for correspondence: tie.wei@nmt.edu

© The Author(s), 2025. Published by Cambridge University Press



https://doi.org/10.1017/jfm.2024.1195 Published online by Cambridge University Press

## 1. Introduction

In the study of boundary layer flows, several thickness parameters are used to characterize the flow, including the displacement thickness $\delta_1$, momentum thickness $\delta_2$, and energy thickness $\delta_3$. These are defined as follows (see Schlichting 1979):

$$\delta_1 \equiv \int_0^\infty \frac{U_\infty - U}{U_\infty}\,\mathrm{d}y, \tag{1.1a}$$

$$\delta_2 \equiv \int_0^\infty \frac{U}{U_\infty}\frac{U_\infty - U}{U_\infty}\,\mathrm{d}y, \tag{1.1b}$$

$$\delta_3 \equiv \int_0^\infty \frac{U}{U_\infty}\frac{U_\infty^2 - U^2}{U_\infty^2}\,\mathrm{d}y = \int_0^\infty \frac{U}{U_\infty}\left(1 + \frac{U}{U_\infty}\right)\frac{U_\infty - U}{U_\infty}\,\mathrm{d}y, \tag{1.1c}$$

where $U$ is the mean velocity in the streamwise $x$-direction, $U_\infty$ is the free-stream velocity, and $y$ denotes the wall-normal direction.

Wieghardt (1948) derived an energy integral equation for laminar boundary layers by multiplying the momentum equation by $U$ and integrating it from $y = 0$ to $y = h > \delta(x)$, where $\delta$ is the boundary layer height. For two-dimensional, laminar boundary layers in incompressible flow, the simplified form of this energy integral equation is given by (see also Schlichting 1979)

$$\frac{1}{2}\frac{\mathrm{d}}{\mathrm{d}x}(U_\infty^3\delta_3) = \nu\int_0^\infty \left(\frac{\partial U}{\partial y}\right)^2 \mathrm{d}y, \tag{1.2}$$

where $\nu$ is the kinematic viscosity. The left-hand side of (1.2) represents the loss in mechanical energy within the boundary layer compared to potential flow, while the right-hand side represents the energy transformed into internal energy due to friction (Wieghardt 1948; Rotta 1953; Schlichting 1979). This equation highlights the importance of energy thickness as a parameter for understanding energy conversion in boundary layer flows.

However, Wieghardt's equation applies only to laminar flows. Despite the dominance of turbulence in most engineering and natural systems, relatively little research has focused on energy thickness in turbulent boundary layers (TBLs). Given the complex nature of TBLs, gaining a deeper understanding of energy thickness in these scenarios is crucial for advancing both theoretical models and practical engineering applications.

The TBLs subjected to pressure gradients are commonly encountered in a wide range of engineering applications, from aircraft wings and turbine blades, to heat exchangers and internal combustion engines. Pressure gradients can significantly alter turbulence characteristics by modifying velocity profiles, vorticity distribution, Reynolds stresses, and turbulent kinetic energy (TKE) production. Understanding these effects is vital for optimizing system performance and efficiency.

In the study of TBLs under pressure gradients, predicting friction coefficients and flow separation has long been a central challenge. One of the most widely used approaches for predicting flow separation is through the boundary layer shape factor, particularly $H_{12} = \delta_1/\delta_2$. This shape factor is an effective metric because it captures the evolution of the boundary layer profile and is highly responsive to changes in the external pressure gradient. When an adverse pressure gradient (i.e. increasing pressure downstream) is present, the shape factor rises, and once it exceeds a critical threshold, flow separation is likely to occur. This concept has been employed widely in both empirical and theoretical investigations into TBLs, as demonstrated in classical studies by researchers such as



https://doi.org/10.1017/jfm.2024.1195 Published online by Cambridge University Press

Stratford (1959), Perry & Schofield (1973), Simpson (1989) and Castillo, Wang & George (2004). While the shape factor $H_{12}$ has proven to be a valuable tool in separation prediction, the role of energy thickness $\delta_3$ in such predictions has been largely overlooked. Energy thickness is intrinsically linked to energy transfer processes in TBLs and could provide deeper insights into the mechanisms that govern flow separation. Recently, Renard & Deck (2016) provided a theoretical decomposition of mean skin friction in TBLs, which was further applied by Senthil *et al.* (2020) to analyse the factors contributing to the skin friction coefficient under adverse pressure gradients. While these studies focus on friction contributions, our work emphasizes the complementary role of energy thickness $\delta_3$ in predicting flow separation.

Another critical aspect of TBLs – whether under pressure gradients or not – is the production of TKE. The production of TKE plays a significant role in energy transfer and turbulent mixing within the flow. However, investigations into the relationship between energy thickness $\delta_3$ and TKE production remain limited in current research. Understanding this relationship could unveil new avenues for enhancing predictions of flow separation across varying pressure gradients. By exploring how $\delta_3$ interacts with TKE, we may gain a better understanding of the mechanisms driving turbulent flow behaviour, thereby refining our predictive models and improving the accuracy of flow separation predictions.

This study aims to address this gap by investigating the role of energy thickness $\delta_3$ in TBLs. We specifically analyse energy thickness in TBLs under zero pressure gradient (ZPG), adverse pressure gradient (APG) and favourable pressure gradient (FPG) conditions. Our findings establish a significant relationship between energy thickness and TKE production in TBLs, and we demonstrate the utility of energy thickness in predicting flow separation and friction coefficients in cases with pressure gradients.

## 2. The TBLs under ZPG

We begin the derivation of the energy integral equation for TBLs over a flat plate. Following Prandtl's boundary layer theory, the mean momentum balance equation in the streamwise direction is

$$0 = -\left[U\frac{\partial U}{\partial x} + V\frac{\partial U}{\partial y}\right] + \nu\frac{\partial^2 U}{\partial y^2} + \frac{\partial R_{uv}}{\partial y}, \tag{2.1}$$

where $R_{uv} = -\langle uv\rangle$ is the kinematic Reynolds shear stress, $u, v$ are the velocity fluctuations in the streamwise and wall-normal directions, respectively, and the angle brackets represent Reynolds averaging. Multiplying the momentum equation by $U$ and integrating it from the wall to the boundary layer edge $\delta_e$ results in

$$-\int_0^{\delta_e} U\left[U\frac{\partial U}{\partial x} + V\frac{\partial U}{\partial y}\right]\mathrm{d}y = \nu\int_0^{\delta_e}\left(\frac{\partial U}{\partial y}\right)^2\mathrm{d}y + \int_0^{\delta_e} R_{uv}\frac{\partial U}{\partial y}\,\mathrm{d}y. \tag{2.2}$$

The definition of $\delta_e$, the boundary layer edge, is somewhat arbitrary (see e.g. von Kármán 1934). A commonly used criterion is to identify $\delta_e$ as the point where the mean streamwise velocity reaches 99 % of the free-stream velocity. Griffin, Fu & Moin (2021) compared several methods for defining boundary layer thickness. To ensure consistency and facilitate experimental data processing, we follow the method proposed by Wei & Knopp (2023), which defines the boundary layer edge as the location where the Reynolds shear stress decreases to 1 % of its maximum value. When resolution near the boundary layer edge is limited, a threshold of 3 % of the maximum value is used. Importantly, due to the slow



https://doi.org/10.1017/jfm.2024.1195 Published online by Cambridge University Press

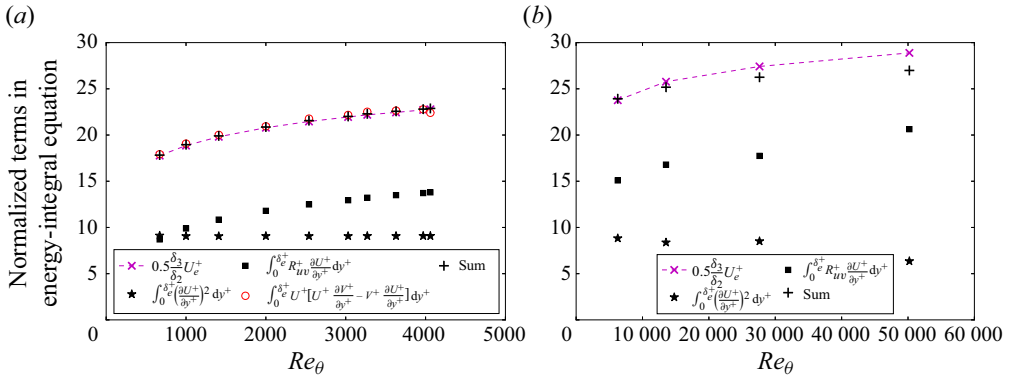



Figure 1. Evaluation of the normalized energy integral (2.2) and the approximation (2.4), where the + symbols represent the sum of the two terms on the right-hand side of (2.4): (*a*) DNS data of Schlatter & Örlü (2010); (*b*) experimental data of Baidya *et al.* (2017, 2021).

variation of flow variables in the outer region, the integrals examined in this study are not highly sensitive to the definition of $\delta_e$.

The left-hand side of (2.2) represents the global integral of the mean streamwise advective force times the streamwise velocity, i.e. the global integral of the power (work per unit time) from the mean advective force to the flow. The mechanical energy input is then lost through viscous dissipation by the mean flow into the internal energy (first term on the right-hand side) and converted to TKE production (second term on the right-hand side). Using the mean wall-normal velocity $V$ profile derived by Wei, Li & Wang (2023*b*) and the relation $U_e V_e/u_\tau^2 \approx \delta_1/\delta_2$ derived by Wei & Klewicki (2016), the energy integral equation for a TBL over a flat plate can be approximated as (see Appendix A for details)

$$\frac{1}{2}\frac{\delta_3}{\delta_2}u_\tau^2 U_e \approx \nu\int_0^{\delta_e}\left(\frac{\partial U}{\partial y}\right)^2 \mathrm{d}y + \int_0^{\delta_e} R_{uv}\frac{\partial U}{\partial y}\,\mathrm{d}y. \tag{2.3}$$

In most experimental or numerical studies of TBLs, data are typically presented in inner scaling, normalized by the friction velocity $u_\tau$ and the viscous length $\nu/u_\tau$ (Tennekes & Lumley 1972). Denoting the inner-scaled variables with a superscript +, the approximate energy integral equation (2.3) can be expressed as

$$\frac{1}{2}\frac{\delta_3}{\delta_2}U_e^+ \approx \int_0^{\delta_e^+}\left(\frac{\partial U^+}{\partial y^+}\right)^2 \mathrm{d}y^+ + \int_0^{\delta_e^+} R_{uv}^+\frac{\partial U^+}{\partial y^+}\,\mathrm{d}y^+. \tag{2.4}$$

Using direct numerical simulations (DNS) data from Schlatter & Örlü (2010), we present the terms from the energy integral (2.2) and its approximation (2.4) in figure 1(*a*). Previous investigations (Laadhari 2007; Abe & Antonia 2016; Wei 2018) have demonstrated that the viscous dissipation by the mean flow is approximately $\int_0^{\delta^+}(\partial U^+/\partial y^+)^2\,\mathrm{d}y^+ \approx 9$ for turbulent channel, pipe or boundary layer flows over a flat plate, seemingly independent of the Reynolds number. This dissipation by the mean flow occurs mainly in the traditional viscous and buffer layers, where the velocity profile $U^+$ exhibits self-similarity with respect to the wall-normal distance $y^+$.

In contrast, the TKE production $\int_0^{\delta_e^+} R_{uv}^+(\partial U^+/\partial y^+)\,\mathrm{d}y^+$ clearly increases with Reynolds number, as shown in figure 1(*a*). The figure demonstrates that the sum of



https://doi.org/10.1017/jfm.2024.1195 Published online by Cambridge University Press

the two terms on the right-hand side of (2.4) (represented by black + symbols) shows excellent agreement with the directly computed value on the left-hand side of the equation (indicated by red circles). Furthermore, the sum also aligns closely with the approximation $0.5\delta_3/\delta_2 U_e^+$ (denoted by magenta × symbols), supporting the validity of the approximate expression in (2.4).

While figure 1(*a*) exhibits excellent agreement with the approximate (2.4), the DNS data used in the figure are at relatively moderate Reynolds numbers. To assess the applicability of the approximate (2.4) at higher Reynolds numbers, figure 1(*b*) incorporates data from experiments conducted by Baidya *et al.* (2017, 2021). In these experiments, the mean wall-normal velocity was not measured, preventing the direct computation of the left-hand side of (2.2) from the experimental data. While the approximate (2.4) shows good agreement at $Re_\theta \approx 6300$ and 13 000 (or $Re_\tau \approx 2500$ and 5000), noticeable deviations are observed at higher Reynolds numbers.

These discrepancies are likely attributed to limitations in experimental resolution, which become increasingly pronounced at higher Reynolds numbers. It is well established that viscous dissipation by the mean shear occurs predominantly in the viscous sub-layer and buffer layer of the ZPG TBL, where TKE production also peaks. To accurately capture dissipation and TKE production in these flows, the viscous sub-layer must be well resolved. However, at high Reynolds numbers, limitations in probe size often result in the first data point falling outside the viscous sub-layer. For example, at $Re_\theta \approx 28\,000$, the first data point is located at $y^+ \approx 8.8$, and at $Re_\theta \approx 50\,000$, it is at $y^+ \approx 25.6$. This under-resolution in the near-wall region leads to underestimations in the calculated integrals, as seen in figure 1(*b*).

To further demonstrate the impact of experimental resolution, we artificially coarsened the data for the lowest Reynolds number case by removing the initial data points, thereby shifting the first data point to $y^+ = 28.2$. This adjustment parallels the conditions at the highest Reynolds number, where the first data point is at $y^+ = 25.6$. Notably, the calculated integral of viscous dissipation continues to exhibit the same underestimation. For brevity, the figure illustrating this adjustment is not included here.

Given the significance of the energy thickness $\delta_3$ in estimating TKE production, figure 2 shows the variation of the ratio $H_{32} = \delta_3/\delta_2$ with Reynolds number in the ZPG TBL. For comparison, the commonly used shape factor $H_{12} = \delta_1/\delta_2$ is also included, demonstrating a clear decrease with increasing Reynolds number. In contrast, the ratio $H_{32}$ exhibits a slower increase with Reynolds number, indicating a weaker dependence.

## 3. The TBLs under pressure gradient

In this study, we primarily use the DNS data by Coleman, Rumsey & Spalart (2018) to validate our analytical results. The DNS study by Coleman *et al.* (2018) investigated non-equilibrium TBLs subjected first to an APG and then to an FPG. In their simulations, pressure gradients were induced using a transpiration profile $V_{top}(x)$ acting through a virtual parallel plane offset by a fixed distance $Y$ from the flat no-slip surface. The archived simulation data were normalized by $Y$ for length and $U_0 = U_e(x_0)$ for velocity.

Figure 3 illustrates the streamwise evolution of flow for case C from the DNS data of Coleman *et al.* (2018). In figure 3(*a*), the variations of normalized boundary layer edge velocities, $U_e/U_0$ and $V_e/U_0$, along with normalized wall pressure, $P_{wall}/(0.5\rho U_0^2)$, are shown. Positive $V_e$ is imposed for $-10 \lesssim x/Y \leq 0$, transitioning to negative for $x/Y > 0$. Analysis of the wall shear stress reveals flow separation in the range $-1.4 \lesssim x/Y \lesssim 0.4$. According to DNS pressure gradient data, the FPG region begins near $x/Y \approx 0.87$. In the



https://doi.org/10.1017/jfm.2024.1195 Published online by Cambridge University Press

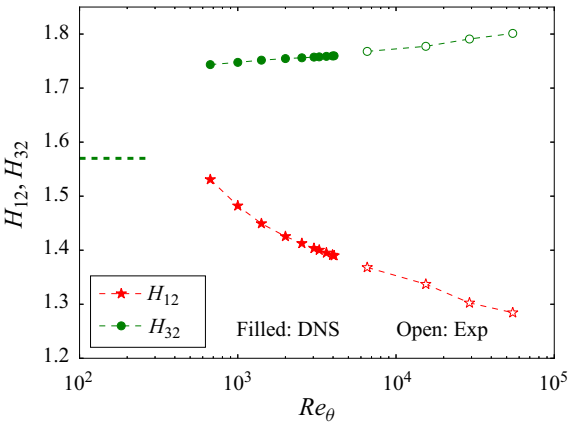



Figure 2. The variation of ratio $H_{32} = \delta_3/\delta_2$ in the ZPG TBL. For laminar flow, the Blasius solution predicts $H_{32} \approx 1.57$. Also shown is the commonly used shape factor $H_{12} = \delta_1/\delta_2$, with laminar value 2.59, for comparison. The data are from DNS by Schlatter & Örlü (2010). The experimental data are from Baidya *et al.* (2021).

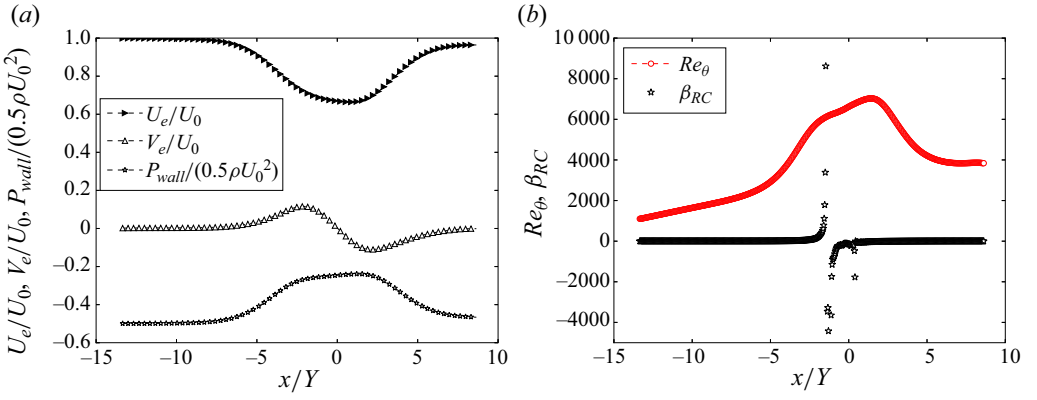



Figure 3. (*a*) Variations of $U_e$, $V_e$ and $P_{wall}$ in the DNS study by Coleman *et al.* (2018). (*b*) Variations of Reynolds number and $\beta_{RC}$. To enhance clarity, not all data points along the $x$-direction are shown.

APG region, $U_e$ decreases to approximately 66 % of the initial free-stream velocity before increasing again in the FPG region.

Figure 3(*b*) shows the streamwise variation of the Reynolds number $Re_\theta = U_e\delta_2/\nu$ and the Rotta–Clauser parameter $\beta_{RC}$, defined as $\beta_{RC} = (\delta_1/(\rho u_\tau^2))\,\mathrm{d}P_e/\mathrm{d}x$. In the study of TBLs under pressure gradient, the Rotta–Clauser parameter is commonly used to measure the strength of the pressure gradient (Clauser 1956; Rotta 1962). The value of $\beta_{RC}$ approaches infinity at the separation points located at $x/Y \approx -1.4$ and $x/Y \approx 0.4$. The Reynolds number in the simulation ranges from 1000 to 7200, with its peak occurring in the FPG region at $x/Y \approx 1.5$.

Figure 4(*a*) presents the variations of the different thicknesses $\delta_e, \delta_1, \delta_2, \delta_3$ in the $x$-direction from the DNS data of Coleman *et al.* (2018). The figure illustrates that $\delta_e$ and $\delta_1$ both increase rapidly under APG and decrease rapidly under FPG in their simulations. Meanwhile, $\delta_2$ and $\delta_3$ also increase under APG and decrease under FPG, but the variation is smaller.



https://doi.org/10.1017/jfm.2024.1195 Published online by Cambridge University Press

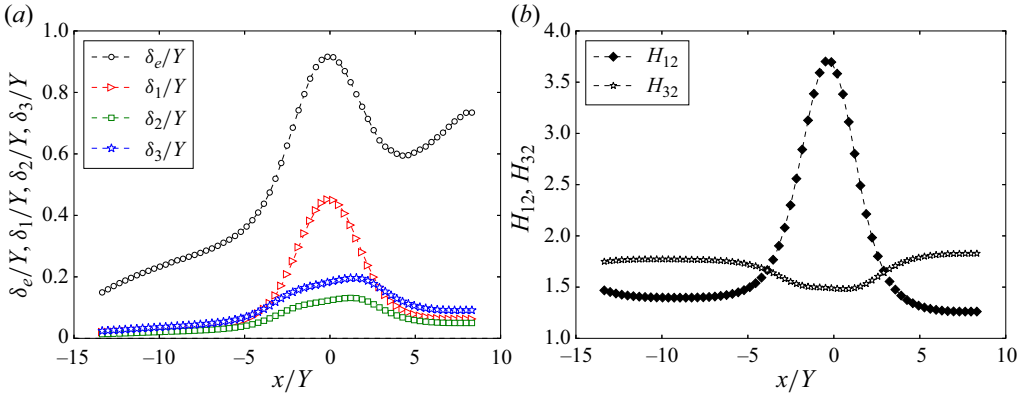



Figure 4. (*a*) Variations of $\delta_e$, $\delta_1$, $\delta_2$, $\delta_3$ in the DNS study by Coleman *et al.* (2018). (*b*) Variations of the ratios $H_{12}$ and $H_{32}$. For clarity, not all data points along the $x$-direction are shown.

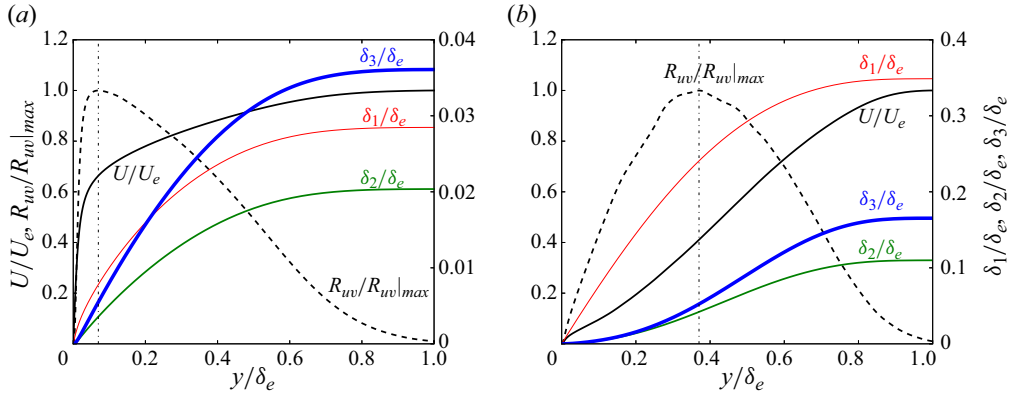



Figure 5. Contributions of different layers to $\delta_1$, $\delta_2$ and $\delta_3$: (*a*) at $x/Y = -10$, where the pressure gradient is negligible, with $Re_\theta \approx 1600$; (*b*) at $x/Y = -1.44$ near the separation point, where $\beta_{RC}$ approaches infinity and $Re_\theta \approx 6100$. The vertical dash-dotted line indicates the peak Reynolds shear stress location $y_m/\delta_e$.

In figure 4(*b*), the ratios of the thicknesses are presented. The commonly used shape factor in TBL studies, $H_{12}$, increases under APG and decreases under FPG. Conversely, the ratio $H_{32}$ varies oppositely, decreasing under APG and increasing under FPG. These ratios have long been recognized as useful descriptors of velocity profiles (see Schlichting 1979). If turbulent velocity profiles can be approximated by a one-parameter family of curves, then $H_{12}$ and $H_{32}$ would be related to each other uniquely (see Schlichting 1979). For instance, assuming power-law velocity profiles, Wieghardt (1945) proposed the relationship $H_{12} = H_{32}/(3H_{32} - 4)$ (see also Schlichting 1979). However, experimental data reveal that the relationship between $H_{12}$ and $H_{32}$ is not unique, as it is influenced by Reynolds number, pressure gradients and flow history, although the deviation from Wieghardt's approximation remains relatively small.

To illustrate the influence of different flow layers, figure 5 shows the cumulative distributions in the calculation of $\delta_1$, $\delta_2$ and $\delta_3$. In figure 5(*a*), the results at $x/Y = -10$ are presented, where the pressure gradient is negligible, with $Re_\theta \approx 1600$ and $\beta_{RC} \approx 0.017$. Figure 5(*b*) shows the results at $x/Y = -1.4$, near the separation point, where $Re_\theta \approx 6100$ with $\beta_{RC} \approx -2.9 \times 10^4$.



https://doi.org/10.1017/jfm.2024.1195 Published online by Cambridge University Press

Based on the force balance characteristics in the mean momentum equation, Wei *et al.* (2005) proposed a four-layer structure for ZPG TBLs and turbulent channel/pipe flows. The peak location of the Reynolds shear stress, $y_m$, represents the centre of layer III (the meso layer) and is indicated by a vertical dash-dotted line in the figure.

Equation (1.1*a*) defines $\delta_1$ as the integral of the mean streamwise velocity deficit $(U_e - U)/U_e$ across the boundary layer, with the velocity deficit reaching its maximum at the wall. Under weak pressure gradients, as shown in figure 5(*a*), the inner regions contribute minimally to $\delta_1$, $\delta_2$ and $\delta_3$ due to their small fraction of the overall boundary layer thickness. For ZPG TBLs, it is established that $y_m \sim 2\delta_e/\sqrt{Re_\tau}$ (see Afzal 1982; Sreenivasan & Sahay 1997; Wei *et al.* 2005). At $x/Y = -10$, $y_m/\delta_e \sim 6\,\%$. In the calculation of $\delta_2$ and $\delta_3$, the velocity deficit is weighted by $U/U_e$ and $U/U_e(1 + U/U_e)$, respectively. These weighting functions further diminish the contribution of the near-wall region, as $U/U_e$ is relatively small in these areas. Due to the different weighting functions, $\delta_3$ will be larger than $\delta_2$, leading to $H_{32}$ being greater than 1.

Under strong APG, the shape of the mean streamwise velocity is influenced significantly, especially in the near-wall region, as shown in figure 5(*b*). Concurrently, the peak location of Reynolds shear stress, $y_m$, moves farther from the wall (see Wei & Knopp 2023), with $y_m/\delta_e \approx 0.4$ at this $x$-location. In the APG regime, the inner regions where the mean streamwise velocity is strongly affected and contribute significantly to $\delta_1$. In contrast, changes in the inner region's velocity profile have less impact on $\delta_2$ and $\delta_3$. This leads to a substantial variation in the shape factor $H_{12}$, as shown in figure 4(*b*), while the variation in $H_{32}$ remains comparatively minor.

In TBL flows, the mass displacement thickness $\delta_1$ is a key parameter in the integral form of the continuity equation, appearing as $V_e = -\delta_e\,\mathrm{d}U_e/\mathrm{d}x + \mathrm{d}(U_e\delta_1)/\mathrm{d}x$ (see Wei *et al.* 2023*a*,*b*), and is linked directly to mass conservation. Similarly, the momentum thickness $\delta_2$ arises in the integral of the streamwise momentum equation (i.e. the von Kármán–Pohlhausen equation) as $\mathrm{d}(U_e^2\delta_2)/\mathrm{d}x$ (see von Kármán 1921; Pohlhausen 1921), making it closely tied to momentum transport and wall shear stress in TBLs. In this study, we extend this framework by demonstrating that the energy thickness $\delta_3$ appears naturally in the integral of the streamwise momentum equation when multiplied by the velocity $U$, in the form $\mathrm{d}(U_e^3\delta_3)/\mathrm{d}x$. This reveals a close connection between $\delta_3$ and the energetic properties of TBLs, offering new insights into energy conversion processes in these flows. By linking energy thickness with TKE production and flow separation, we provide a more comprehensive understanding of boundary layer behaviour, particularly in the presence of pressure gradients.

### 3.1. *Friction coefficient in TBLs under pressure gradients*

One of the primary goals in the study of TBLs is predicting the wall shear stress or friction coefficient $C_f = \tau_{wall}/(0.5\rho U_e^2) = 2u_\tau^2/U_e^2$, where $\tau_{wall}$ is the local wall shear stress, and $U_e$ is the mean streamwise velocity at the boundary layer edge. While accurate prediction models for $C_f$ have been developed for ZPG TBLs, predicting $C_f$ under pressure gradients, and particularly determining the location where the wall shear stress becomes zero (i.e. the separation point), remains a challenge. Figure 6(*a*) presents the variations of $C_f$ and $H_{32}$ in the $x$-direction from the DNS data of Coleman *et al.* (2018). In ZPG TBLs, $H_{32}$ exceeds 1.7, and its value increases gradually with Reynolds numbers (see figure 2). However, under APG conditions, the value of $H_{32}$ decreases below the ZPG values. Specifically, figure 6(*a*) demonstrates that the wall shear stress reaches zero at approximately the location where $H_{32}$ drops below 1.48.



https://doi.org/10.1017/jfm.2024.1195 Published online by Cambridge University Press

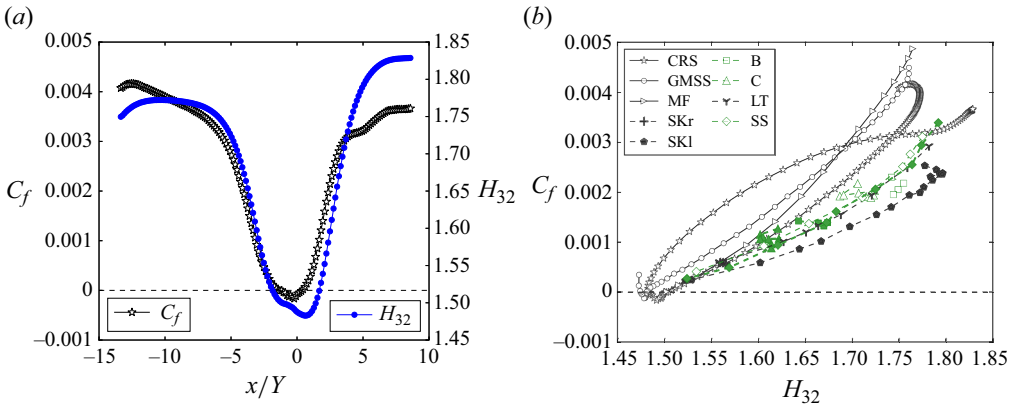



Figure 6. (*a*) Variation of friction coefficient $C_f$ and $H_{32}$ using DNS data from Coleman *et al.* (2018). (*b*) Comparison of $C_f$ and $H_{32}$ with DNS data from Coleman *et al.* (2018) (CRS), from Gungor *et al.* (2016) (GMSS) and from Manhart & Friedrich (2002) (MF), and experimental data from Skåre & Krogstad (1994) (SKr), from Schubauer & Klebanoff (1951) (SKl), from Bradshaw (1965, 1966) (B; open, mild APG; filled, moderate APG), from Clauser (1954) (C; open, mild APG; filled, moderate APG), from Ludwieg & Tillmann (1949) (LT) and from Schubauer & Sprangenberg (1960) (SS; open, ID 4500; filled, ID 4800).

To explore the relationship between $C_f$ and $H_{32}$, we conducted an extensive analysis that included a wide range of experimental data along with DNS data. This comprehensive dataset included equilibrium and streamwise-evolving cases from the compilation by Coles & Hirst (1969), with the same identifiers (ID) used for reference. We examined equilibrium TBL flows under mild APG from Bradshaw (1966) (ID 2500) and moderate APG from Bradshaw (1965) (ID 2600). Additionally, we studied equilibrium boundary layer flows under mild APG (ID 2200) and moderate APG (ID 2300) from Clauser (1954). Streamwise evolving flows under strong APG (ID 1200) from Ludwieg & Tillmann (1949), as well as flows B (ID 4500) and E (ID 4800) from Schubauer & Sprangenberg (1960), were also part of our analysis. Furthermore, we considered the TBL flow over a large aerofoil-like body from Schubauer & Klebanoff (1950), which involves small surface curvature and history effects. This flow scenario includes an initial phase under a strong FPG in the nose region, transitioning to a mild FPG, and finally encountering an APG region.

In the dataset compiled by Coles & Hirst (1969), the boundary layer thickness $\delta$, the wake factor $\Pi$, and the friction velocity $u_\tau$ were determined by minimizing the root mean square deviation of the data from the law-of-the-wall/law-of-the-wake:

$$u^+ = \frac{1}{\kappa}\log(y^+) + B + \frac{2\Pi}{\kappa}\left(\sin\left(\frac{\pi\eta}{2}\right)\right)^2, \quad \eta = \frac{y}{\delta}, \tag{3.1}$$

using $\kappa = 0.41$ and $B = 5.0$. For the calculation of the integral thicknesses, an analytical wall law for the mean velocity was applied between the wall and the first data point, as describe in Coles & Hirst (1969).

Figure 6(*b*) illustrates the variation of $C_f$ with $H_{32}$ under different pressure gradient conditions. It shows that the manner in which the APG is applied influences the rate at which $C_f$ decreases with $H_{32}$. Nevertheless, the figure clearly indicates that $C_f$ approaches zero, signifying the separation point, at $H_{32} \approx 1.48$, regardless of the specific method of APG imposition. This consistency suggests that $H_{32}$ has potential as a reliable criterion for predicting flow separation.



https://doi.org/10.1017/jfm.2024.1195 Published online by Cambridge University Press

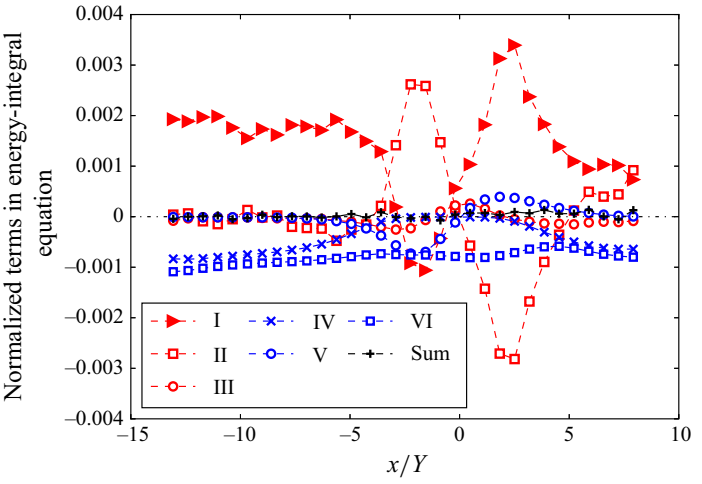



Figure 7. Terms in the energy integral (3.2). Data are from DNS data of Coleman *et al.* (2018). Note that velocity in the DNS data is normalized by the free-stream velocity at the simulation inlet, and distance is normalized by the domain size in the wall-normal direction.

### 3.2. *Energy integral equation for TBLs under pressure gradients*

The energy integral equation for TBLs under arbitrary pressure gradients can be obtained as follows (detailed in Appendix B):

$$0 = \underbrace{\frac{1}{2}\frac{\mathrm{d}}{\mathrm{d}x}(U_e^3\delta_3)}_{\mathrm{I}} \underbrace{-\int_0^{\delta_e}\left(\frac{1}{\rho}\frac{\partial P}{\partial x}+U_e\frac{\mathrm{d}U_e}{\mathrm{d}x}\right)U\,\mathrm{d}y}_{\mathrm{II}} + \underbrace{\frac{\mathrm{d}}{\mathrm{d}x}\int_0^{\delta_e}UR_{uu}\,\mathrm{d}y}_{\mathrm{III}}$$
$$\underbrace{-\nu\int_0^{\delta_e}\left(\frac{\partial U}{\partial y}\right)^2\mathrm{d}y}_{\mathrm{IV}} \underbrace{-\int_0^{\delta_e}R_{uu}\frac{\partial U}{\partial x}\,\mathrm{d}y}_{\mathrm{V}} \underbrace{-\int_0^{\delta_e}R_{uv}\frac{\partial U}{\partial y}\,\mathrm{d}y}_{\mathrm{VI}}. \tag{3.2}$$

Here, the sum of terms I and II represents the energy exchange from the mean advective and pressure forces. Term III arises from the gradient of Reynolds normal stress $\partial R_{uu}/\partial x$. Term IV represents the viscous dissipation into internal energy by the mean shear, while terms V and VI are the TKE production terms, i.e. they convert mean kinetic energy to turbulence kinetic energy. In the case of the ZPG TBL, term II vanishes. For the ZPG laminar boundary layer, terms II, III, V, VI are zero, and the Wieghardt equation (1.2) is reproduced.

The terms in (3.2) are illustrated in figure 7 using DNS data from Coleman *et al.* (2018). The non-smoothness observed in the data for terms I and II can be attributed to the computation of $x$-derivatives during the post-processing stage. Despite this, the residual remains close to zero, with any deviation likely arising from the calculation of $x$-derivatives in the post-processing stage.

Figure 7 demonstrates that under strong pressure gradients, term II becomes significant and cannot be neglected. This observation aligns with the findings in Wei, Li & Wang (2024), which emphasize the substantial deviation of $-\partial(P_{wall}/\rho)/\partial x$ from $U_e\,\mathrm{d}U_e/\mathrm{d}x$ under such conditions. Consequently, the original Wieghardt equation (1.2) becomes invalid under strong pressure gradients.



https://doi.org/10.1017/jfm.2024.1195 Published online by Cambridge University Press

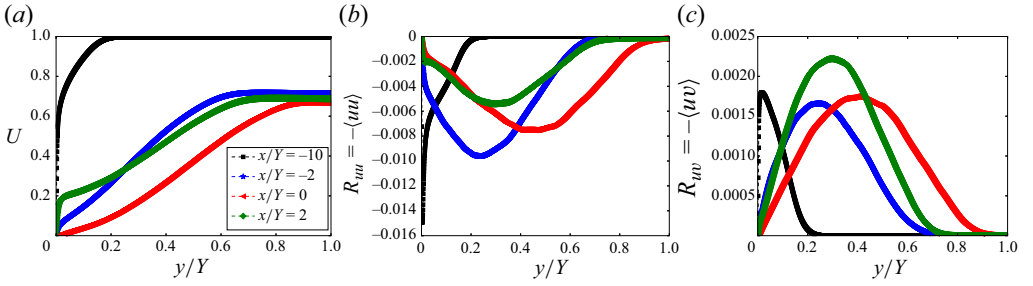



Figure 8. Effects of varying pressure gradients on the profiles of $U$, $R_{uu}$ and $R_{uv}$. The Reynolds number and Rotta–Clauser parameters at the four $x$-stations are ($Re_\theta = 1620$, $\beta_{RC} = 0.017$), ($Re_\theta = 5770$, $\beta_{RC} = 157$), ($Re_\theta = 6600$, $\beta_{RC} = -147$) and ($Re_\theta = 6800$, $\beta_{RC} = -23$) for $x/Y = -10, -2, 0, 2$, respectively. The DNS data are from Coleman *et al.* (2018).

### 3.3. *Approximations for the terms in the energy integral equation*

In numerical simulations of TBL, the terms in (3.2) can be determined directly and precisely from the simulation data, assuming that adequate numerical resolutions are employed. However, in physical experiments, the resolution is often constrained, particularly in the vicinity of the wall. Additionally, in typical hot-wire experiments, the number of measurements across various $x$-stations is limited. Therefore, the development of approximations for the terms in the energy integral equations becomes valuable, particularly for those terms that are difficult to obtain experimentally. Even a rough estimation of the order of magnitude would be useful for gaining further insights. Moreover, an investigation of the scaling of the different terms using characteristic boundary layer quantities is of interest. The goal is to reveal boundary layer parameters other than the popular parameters like $H_{12}$, which characterize the local state of the boundary layer and how susceptible the flow is to flow separation.

To gain a better understanding of the terms in (3.2), we first analyse the effects of the pressure gradient on the shapes of the mean flow and Reynolds stresses in the wall-normal direction. Subsequently, we present the distribution of the variables within the integrals in (3.2), allowing us to appreciate the contributions of different regions of the TBL to the overall integrals.

The pressure gradient directly affects the shape of the mean flow and the distribution of Reynolds stresses. Figure 8 illustrates the variations in mean streamwise velocity $U$, Reynolds normal stress $R_{uu}$, and Reynolds shear stress $R_{uv}$ at four distinct $x$-locations, each experiencing different intensities of pressure gradients. Under zero or weak pressure gradients, $U$ exhibits a steep slope in the near-wall region. The magnitudes of Reynolds normal or shear stresses also peaks in the near-wall region. However, under strong APG, the slope of $U$ in the near-wall region diminishes significantly, becoming zero at the separation point. The peak locations of the Reynolds stresses also shift towards the centre of the TBL (see also Wei & Knopp 2023).

The variations in the mean flow and Reynolds stress profiles, induced by pressure gradients, lead to significant changes in the contributions of different regions within the TBL to dissipation and TKE production. To better show the near-wall region, figure 9 depicts the pre-multiplied dissipation and TKE productions plotted on semi-logarithmic axes. Under weak pressure gradients, the viscous dissipation is concentrated predominantly in the near-wall region, specifically the viscous and buffer sub-layers. However, under strong APG, the viscous dissipation shifts significantly to the outer region, due to the diminishing slope of the mean velocity profile $U$ in the near-wall



https://doi.org/10.1017/jfm.2024.1195 Published online by Cambridge University Press

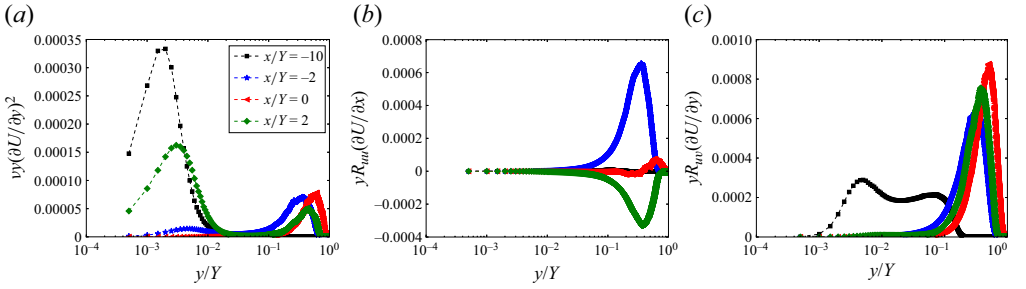



Figure 9. (*a*) Pre-multiplied viscous dissipation profiles. To enhance visibility, the values at $x/Y = -2$, 0 and 2 have been multiplied by a factor of 10, due to their actual values being significantly smaller compared to that at $x = -10$. (*b*) Pre-multiplied TKE production by $R_{uu}\,\partial U/\partial x$. (*c*) Pre-multiplied TKE production by $R_{uv}\,\partial U/\partial y$. The DNS data are from Coleman *et al.* (2018).

region. Analogously, the contribution of the outer region to TKE production also gains prominence under strong APG conditions due to the increase of $\partial U/\partial y$ in the case of a large mean-velocity deficit in the outer layer (Gungor *et al.* 2016; Maciel *et al.* 2018)

It is well known that the inner normalized mean streamwise velocity $U^+(y^+)$ in the ZPG TBL exhibits a self-similarity in the viscous and buffer layers (see Tennekes & Lumley 1972; Monin & Yaglom 1965). Hence the viscous dissipation term in the ZPG TBL can be estimated as

$$\nu \int_0^{\delta_e} (\partial U/\partial y)^2 \,\mathrm{d}y = u_\tau^3 \int_0^{\delta_e^+} (\partial U^+/\partial y^+)^2 \,\mathrm{d}y^+ \approx u_\tau^3 \int_0^{20} (\partial U^+/\partial y^+)^2 \,\mathrm{d}y^+ \approx c\, u_\tau^3. \tag{3.3}$$

The constant turns out to be approximately 9 (see figure 1). However, under pressure gradients, the inner-scaled $U^+$ is not self-similar in the near-wall region. Moreover, the dissipation by the mean shear is not concentrated in the near-wall region either. Figure 7 reveals that term IV decreases with the magnitude of the wall shear stress, eventually approaching zero in the separated region ($-1.4 \lesssim x/Y \lesssim 0.4$). Based on the DNS data of Coleman *et al.* (2018) shown in figure 10(*a*), the viscous dissipation by the mean shear can be approximated as

$$-\nu \int_0^{\delta_e} \left(\frac{\partial U}{\partial y}\right)^2 \mathrm{d}y \sim -0.22\,\frac{\delta_3}{\delta_2}\,u_\tau^2 U_e. \tag{3.4}$$

To further assess the validity of the approximation (3.4), figure 10(*b*) presents data from independent DNS studies by Gungor, Maciel and colleagues (Gungor *et al.* 2016; Gungor, Maciel & Gungor 2022; Gungor, Gungor & Maciel 2024). These studies included three simulations of highly non-equilibrium TBLs evolving under a pressure gradient. The publicly accessible data comprise information at eight streamwise positions for each simulation. As figure 10(*b*) illustrates, the approximation (3.4) exhibits good agreement with the three datasets. However, the underlying physical rationale for this empirical approximation (3.4) remains elusive. Notably, the functional form of (3.4) exhibits a resemblance to the left-hand side of (2.3), suggesting potential connections or analogies between the two expressions. Further investigation is warranted to elucidate the physical basis of this approximation and its applicability in various flow conditions.

To gain insight into and compare the TKE production terms V and VI, figure 11(*a*) presents the ratio between $V_e$ and $U_e$ obtained from the DNS data of Coleman *et al.* (2018). Figure 11(*b*) presents the ratios between the averaged Reynolds normal stress and Reynolds



https://doi.org/10.1017/jfm.2024.1195 Published online by Cambridge University Press

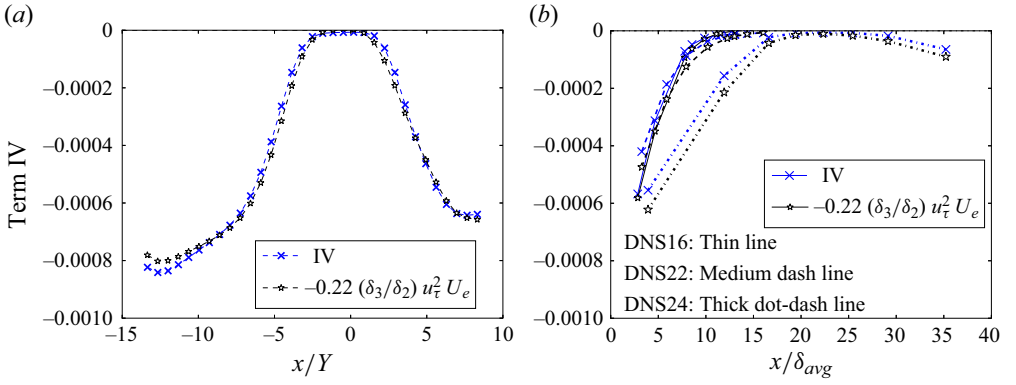



Figure 10. Molecular dissipation by mean shear term: (*a*) DNS data of Coleman *et al.* (2018); (*b*) DNS data of Gungor *et al.* (2016, 2022, 2024).

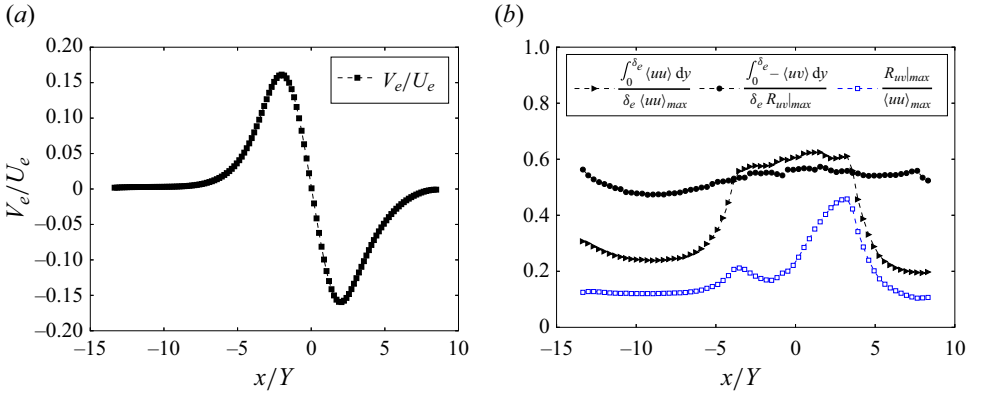



Figure 11. (*a*) Ratio of $V_e$ to $U_e$ obtained from the DNS data of Coleman *et al.* (2018). (*b*) Ratios of the average Reynolds normal stress and Reynolds shear stress to the maximum Reynolds shear stress.

shear stress to the maximum Reynolds stresses. Under zero or weak pressure gradients, the mean wall-normal velocity $V_e$ is significantly smaller than the streamwise velocity $U_e$, resulting in a very small $V_e/U_e$ ratio. This indicates that the boundary layer remains thin. However, under strong pressure gradients, $V_e$ approaches the magnitude of $U_e$, as shown in figure 11(*a*).

Figure 11(*b*) demonstrates that, regardless of the pressure gradient, the averaged Reynolds shear stress remains approximately half of the maximum Reynolds shear stress. However, the ratio between the averaged Reynolds normal stress $\langle uu\rangle$ and $\langle uu\rangle_{max}$ exhibits a dependence on the pressure gradient. Specifically, under a weak pressure gradient, this ratio is approximately 0.24. Near the separation point, this ratio increases to approximately 0.6. Furthermore, the ratio between the maximum Reynolds shear stress and $\langle uu\rangle_{max}$ also exhibits a pressure gradient dependence. Under weak pressure gradients, this ratio is approximately 0.12, but it can increase to approximately 0.5 under strong pressure gradients. Despite these variations, figure 11(*b*) illustrates that $\langle uu\rangle_{max}$ remains of the same order of magnitude as the maximum Reynolds shear stress. It is noteworthy that in high Reynolds number ZPG TBLs, the maximum Reynolds shear stress is approximately $u_\tau^2$.



https://doi.org/10.1017/jfm.2024.1195 Published online by Cambridge University Press

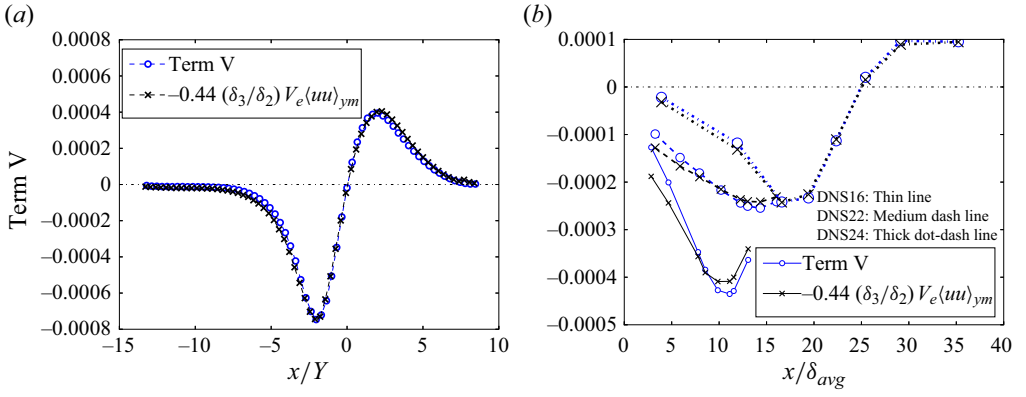



Figure 12. Approximation of the TKE production from $R_{uu}\,\partial U/\partial x$: (*a*) DNS data of Coleman *et al.* (2018); (*b*) DNS data of Gungor *et al.* (2016, 2022, 2024).

Figure 7 illustrates that term V in (3.2), representing the TKE 'production' by $R_{uu}\partial U/\partial x$, is insignificant under weak pressure gradients. However, under strong pressure gradients and significant streamwise changes of the wall shear stress, this term approaches the magnitude of the production resulting from $R_{uv}\,\partial U/\partial y$. On the other hand, for flows near equilibrium with a small streamwise change of the wall shear stress, the contribution is much smaller, as shown in figure 9 of Skåre & Krogstad (1994). Furthermore, term V becomes positive under strong FPG, indicating a conversion of TKE to mean kinetic energy. The sum of terms V and VI remains negative, indicating an overall net conversion of mean kinetic energy into TKE across the entire domain of the DNS conducted by Coleman *et al.* (2018).

Based on the DNS data of Coleman *et al.* (2018) shown in figure 12, the term V in (3.2) can be approximated as

$$-\int_0^{\delta_e} R_{uu}\,\frac{\partial U}{\partial x}\,\mathrm{d}y = \int_0^{\delta_e} R_{uu}\,\frac{\partial V}{\partial y}\,\mathrm{d}y \approx -0.44\,\frac{\delta_3}{\delta_2}\,V_e\langle uu\rangle_{y_m}. \tag{3.5}$$

Figure 12(*b*) shows that the approximate (3.5) also works reasonably well for the DNS data of Gungor *et al.* (2016, 2022, 2024). This approximation underscores the significance of $V_e$ and $\langle uu\rangle_{y_m}$, as well as the importance of the thicknesses $\delta_2$, $\delta_3$, in estimating the TKE production by $R_{uu}\,\partial U/\partial x$.

Under weak pressure gradients, where $V_e$ is significantly smaller than $U_e$ as shown in figure 11(*a*), the TKE production by $R_{uu}\,\partial U/\partial x$ is therefore considerably smaller than that by $R_{uv}\,\partial U/\partial y$. However, under strong pressure gradients, the magnitudes of $V_e$ and $U_e$ become comparable. Additionally, as shown in figure 11(*b*), $\int_0^{\delta_e}\langle uu\rangle\,\mathrm{d}y$ is larger than $\int_0^{\delta_e} R_{uv}\,\mathrm{d}y$. Consequently, under strong pressure gradients, the TKE production by $R_{uu}\,\partial U/\partial x$ becomes comparable in magnitude to that from $R_{uv}\,\partial U/\partial y$, as shown in figure 7.

Figure 7 shows that term VI, the integral of TKE production by $R_{uv}\,\partial U/\partial y$, exhibits relatively small variations throughout the simulation domain, despite the presence of substantial changes in the pressure gradient. Notably, term VI remains negative across different pressure gradients, indicating that it extracts energy from the mean flow to TKE. Furthermore, figure 13 indicates that the TKE production under weak pressure gradients



https://doi.org/10.1017/jfm.2024.1195 Published online by Cambridge University Press

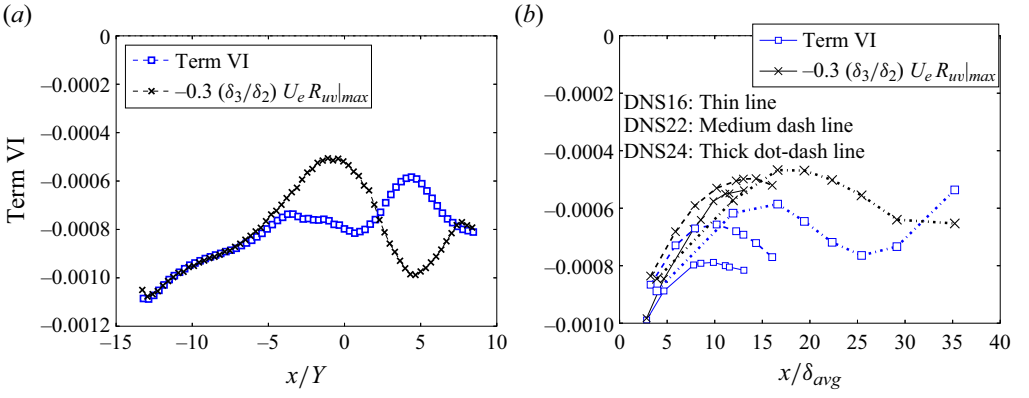



Figure 13. Estimation of TKE production by $R_{uv}\,\partial U/\partial y$: (*a*) DNS data of Coleman *et al.* (2018); (*b*) DNS data of Gungor *et al.* (2016, 2022, 2024).

by $R_{uv}\,\partial U/\partial y$ can be estimated as

$$-\int_0^{\delta_e} R_{uv}\,\frac{\partial U}{\partial y}\,\mathrm{d}y \sim -0.3\,\frac{\delta_3}{\delta_2}\,U_e\,R_{uv}|_{max}. \tag{3.6}$$

However, this estimation loses validity under strong pressure gradients. Nonetheless, it still provides a reasonable estimate of the order of magnitude of the TKE production by $R_{uv}\,\partial U/\partial y$, as corroborated by independent DNS data from Gungor *et al.* (2016, 2022, 2024). Additionally, validation with experimental data from Skåre & Krogstad (1994) shows excellent support for the approximation in (3.6), with the numerical factor varying between 0.3 and 0.35 across seven $x$-stations, averaging 0.32.

### 3.4. *Normalization of the energy integral equation*

In approximating the terms in the energy integral equation (§ 3.3), the factor $(\delta_3/\delta_2)U_e\,R_{uv}|_{max}$ assumes a crucial role. This scaling factor can be used effectively to normalize the energy integral (3.2). The outcomes of this normalization are displayed in figure 14, providing a clearer visualization of the relative contributions of the various terms within the equation. In figure 14(*a*), the black + symbols represent the direct sum of terms I–VI calculated using DNS data, while the magenta × symbols represent the sum where terms IV, V and VI are approximated using (3.4), (3.5) and (3.6), respectively. The approximate sum closely aligns with zero under weak pressure gradients, but exhibits notable deviations under strong pressure gradients, primarily due to the limitations of the approximate equation (3.6) in such conditions.

To further elucidate the combined effect of the advective term and pressure term, terms I and II are combined in figure 14(*b*). Both figures demonstrate that the normalized terms are of or smaller than $O(1)$, indicating their relative magnitudes and significance within the energy integral equation.

Under zero or weak pressure gradient, the normalized term I approximates 0.5, which aligns with the left-hand side of (2.3). Note that in high Reynolds number ZPG TBLs, the maximum Reynolds shear stress $R_{uv}|_{max}$ closely approximates the square of the friction velocity $u_\tau^2$.

Figure 14(*b*) shows that in the presence of strong APG, the advective and pressure forces (sum of terms I and II in (3.2)) augment the injection of mechanical energy into



https://doi.org/10.1017/jfm.2024.1195 Published online by Cambridge University Press

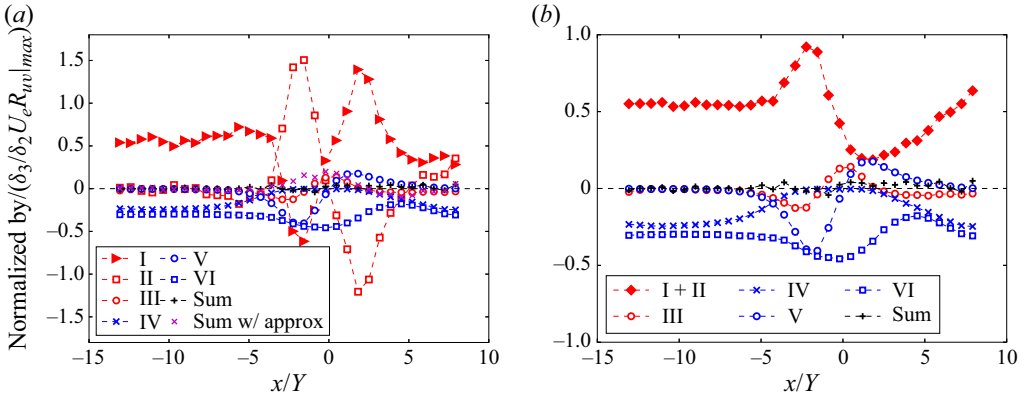



Figure 14. (*a*) Energy integral equation (3.2) normalized by $(\delta_3/\delta_2)U_e R_{uv}|_{max}$. Black + symbols represent the sum of terms I–VI calculated using DNS data, whereas magenta x symbols represent the sum of terms I–III calculated using DNS data and terms IV–VI estimated using approximate equations. (*b*) Combined contributions of terms I and II. The DNS data are from Coleman *et al.* (2018).

the flow. This additional energy is then converted to TKE mainly by the term $R_{uu}\,\partial U/\partial x$ (term V). Conversely, under strong FPG ($0.2 \lesssim x/Y \lesssim 5$), there is a noticeable decrease in the injection of the mechanical energy, leading to a corresponding reduction in TKE production by $R_{uv}\,\partial U/\partial y$ (term VI). Moreover, the term $R_{uu}\,\partial U/\partial x$ (term V) reverses its role, converting TKE back to mechanical energy under strong FPG.

Utilizing the scaling factor, the relative contribution of the viscous dissipation term IV is related to the ratio $u_\tau^2/R_{uv}|_{max}$. Under strong APG, particularly in proximity to the separation point, this ratio undergoes a substantial decrease, resulting in a significant reduction in the viscous dissipation. The contribution of the normalized term V can be assessed by the factor $V_e/U_e$, which typically remains negligible small, except in regions under strong pressure gradients.

## 4. Summary

In this work, we have derived a novel energy integral equation for zero pressure gradient (ZPG) turbulent boundary layers (TBLs). This equation introduces a precise approximation of the combined dissipation resulting from mean shear and TKE production, formulated as $0.5(\delta_3/\delta_2)u_\tau^2 U_e$. This approximation, free from $x$-derivatives, offers a practical alternative for estimating TKE production in physical experiments, where the measurements are typically limited to select $x$-stations, and the direct measurement of Reynolds shear stress can be challenging. The accuracy and robustness of our newly derived approximate equation for ZPG TBLs have been validated through comprehensive comparisons with the DNS and experimental data across a wide range of Reynolds numbers.

For TBLs subjected to pressure gradients, the significance of the energy thickness becomes more prominent. Our analysis of multiple independent DNS and experimental datasets, encompassing TBLs under various pressure gradients, reveals a consistent and robust correlation between the friction coefficient $C_f$ and the ratio $H_{32} = \delta_3/\delta_2$. This correlation highlights the potential of using $H_{32}$ as an alternative, readily obtainable parameter in predicting flow separation under strong adverse pressure gradients. In addition, we have rigorously derived a novel energy integral equation for the TBL under arbitrary pressure gradients, where $\delta_3$ retains its significance. The behaviour



https://doi.org/10.1017/jfm.2024.1195 Published online by Cambridge University Press

of all the terms in the energy integral equation for the TBL under varying pressure gradients is investigated by using high-fidelity DNS data. Furthermore, to enhance practical applicability, we propose approximate equations for the dissipation due to the mean shear and TKE productions resulting from Reynolds normal and shear stresses, explicitly incorporating $\delta_3$. The accuracy and reliability of these approximate equations are confirmed through validation against diverse DNS datasets.

Our investigation also reveals that under mild pressure gradients, the TKE production by $R_{uu}\,\partial U/\partial x$ is negligible compared to that by $R_{uv}\,\partial U/\partial y$. However, in the presence of strong pressure gradients, the production by $R_{uu}\,\partial U/\partial x$ becomes comparable in magnitude to that by $R_{uv}\,\partial U/\partial y$. While the TKE production by $R_{uv}\,\partial U/\partial y$ remains consistently positive under all pressure gradients, the production by $R_{uu}\,\partial U/\partial x$ reverses sign under a strong favourable pressure gradient, indicating a conversion of TKE to mean kinetic energy. These observations provide valuable insights into the intricate physics governing TBLs under pressure gradients, advancing our understanding of their behaviour and dynamics.

**Acknowledgements.** We express our gratitude to Dr Coleman, Dr Gungor, and Dr Maciel for generously sharing their DNS data. The DNS dataset from Coleman *et al.* (2018) is archived in the NASA Turbulence Modeling Resource (TMR) at https://turbmodels.larc.nasa.gov/Other_DNS_Data/separation_bubble_2d.html.

**Declaration of interests.** The authors report no conflict of interest.

**Author ORCIDs.**
Tie Wei https://orcid.org/0000-0001-7256-6052;
Tobias Knopp https://orcid.org/0000-0002-3161-5353;
Zhaorui Li https://orcid.org/0000-0003-1858-2857.

## Appendix A. Derivation of the energy integral equation for ZPG TBLs

The advective terms in the mean momentum equation, when multiplied by $U$, yield

$$-U\left[U\frac{\partial U}{\partial x}+V\frac{\partial U}{\partial y}\right]=U\left[U\frac{\partial V}{\partial y}-V\frac{\partial U}{\partial y}\right]=\frac{3}{2}U^2\frac{\partial V}{\partial y}-\frac{1}{2}\frac{\partial (U^2V)}{\partial y}. \tag{A1}$$

The integral of the second term on the right-hand side is trivial. To obtain the integral of the first term on the right-hand side, we first transform the equation into a dimensionless form using the normalized variables defined as (see Wei *et al.* 2023*b*)

$$U^-\equiv\frac{U_e-U}{U_e},\quad V^-\equiv\frac{V}{V_e},\quad y^-\equiv\frac{y}{\delta_e}. \tag{A2$a$–$c$}$$

Substituting the normalized variables, the term $U^2\,\partial V/\partial y$ can be expressed as

$$U^2\frac{\partial V}{\partial y}=\frac{U_e^2V_e}{\delta_e}\left(1-2U^-+(U^-)^2\right)\frac{\partial V^-}{\partial y^-}. \tag{A3}$$

Wei *et al.* (2023*b*) derived an approximate equation for

$$\frac{\partial V^-}{\partial y^-}\approx-\frac{\delta_e}{\delta_1}y^-\frac{\partial U^-}{\partial y^-}, \tag{A4}$$



https://doi.org/10.1017/jfm.2024.1195 Published online by Cambridge University Press

which transforms the above equation to

$$U^2\frac{\partial V}{\partial y} \approx -\frac{U_e^2V_e}{\delta_1}\left\{\frac{\partial}{\partial y^-}(y^-U^-) - U^- - \frac{\partial}{\partial y^-}(y^-(U^-)^2) + (U^-)^2 + \frac{1}{3}\frac{\partial}{\partial y^-}(y^-(U^-)^3) - \frac{1}{3}(U^-)^3\right\}. \tag{A5}$$

Using the approximate (A5), the integral of (A1) from $y = 0$ to $y = \delta_e$ becomes

$$\begin{aligned} -\int_0^{\delta_e} U\left[U\frac{\partial U}{\partial x} + V\frac{\partial U}{\partial y}\right]\mathrm{d}y &= \int_0^{\delta_e}\frac{3}{2}U^2\frac{\partial V}{\partial y}\,\mathrm{d}y - \int_0^{\delta_e}\frac{1}{2}\frac{\partial(U^2V)}{\partial y}\,\mathrm{d}y \\ &\approx -\frac{3}{2}U_e^2V_e\frac{\delta_e}{\delta_1}\left(-\int_0^1(U^-)\,\mathrm{d}y^- + \int_0^1(U^-)^2\,\mathrm{d}y^- - \frac{1}{3}\int_0^1(U^-)^3\,\mathrm{d}y^-\right) - \frac{1}{2}U_e^2V_e \\ &= -\frac{3}{2}U_e^2V_e\frac{\delta_e}{\delta_1}\left(-\frac{\delta_1}{\delta_e} + \frac{\delta_1-\delta_2}{\delta_e} - \frac{1}{3}\frac{\delta_1+\delta_3-3\delta_2}{\delta_e}\right) - \frac{1}{2}U_e^2V_e \\ &= \frac{1}{2}\frac{\delta_3}{\delta_1}U_e^2V_e. \end{aligned} \tag{A6}$$

Wei & Klewicki (2016, 2023) have found that $U_eV_e$ at high Reynolds numbers of ZPG TBLs can be approximated as

$$U_eV_e \approx H_{12}u_\tau^2, \tag{A7}$$

which leads to an approximation

$$-\int_0^{\delta_e} U\left[U\frac{\partial U}{\partial x} + V\frac{\partial U}{\partial y}\right]\mathrm{d}y \approx \frac{1}{2}\frac{\delta_3}{\delta_2}u_\tau^2U_e. \tag{A8}$$

This approximation equation is supported by the DNS data of Schlatter & Örlü (2010), as shown in figure 1. This suggests a close relationship between the energy input from the advective force in the streamwise direction and parameters such as the energy thickness and momentum thickness, as well as the wall shear stress $u_\tau^2$ and $U_e$.

## Appendix B. Derivation for the energy integral equation in the *x*-direction for a TBL under a pressure gradient

The derivation of the energy integral for a TBL under a pressure gradient is more tedious, but the steps are the same. We start with the mean momentum equation for a TBL under a pressure gradient (see Wei *et al.* 2024):

$$0 = -\left[U\frac{\partial U}{\partial x} + V\frac{\partial U}{\partial y}\right] + \nu\frac{\partial^2U}{\partial y^2} - \frac{1}{\rho}\frac{\partial P}{\partial x} + \frac{\partial R_{uv}}{\partial y} + \frac{\partial R_{uu}}{\partial x}. \tag{B1}$$

In a TBL under zero or weak pressure gradients, the term $\partial R_{uu}/\partial x$ is typically negligible. However, under a strong APG, it becomes non-negligible.

The energy integral equation is obtained by multiplying the $x$-momentum equation by $U$ and integrating from $y = 0$ to $y = \delta_e$. The integration of the viscous and Reynolds shear



https://doi.org/10.1017/jfm.2024.1195 Published online by Cambridge University Press

stress terms is straightforward. Utilizing integration by parts and the Leibniz integral rule, the integral $\int_0^{\delta_e}(U\,\partial R_{uu}/\partial x)\,\mathrm{d}y$ can be expressed as

$$\begin{aligned}\int_0^{\delta_e} U\,\frac{\partial R_{uu}}{\partial x}\,\mathrm{d}y &= \int_0^{\delta_e}\frac{\partial(UR_{uu})}{\partial x}\,\mathrm{d}y - \int_0^{\delta_e} R_{uu}\,\frac{\partial U}{\partial x}\,\mathrm{d}y \\ &= \frac{\mathrm{d}}{\mathrm{d}x}\int_0^{\delta_e} UR_{uu}\,\mathrm{d}x - \int_0^{\delta_e} R_{uu}\,\frac{\partial U}{\partial x}\,\mathrm{d}y,\end{aligned} \tag{B2}$$

which corresponds to terms III and V in (3.2).

The integral $\int_0^{\delta_e} -U[U\,\partial U/\partial x + V\,\partial U/\partial y]\,\mathrm{d}y$ can be expressed as

$$\begin{aligned}&\int_0^{\delta_e} -U\left[U\,\frac{\partial U}{\partial x} + V\,\frac{\partial U}{\partial y}\right]\mathrm{d}y = -\int_0^{\delta_e} U^2\,\frac{\partial U}{\partial x}\,\mathrm{d}y + \frac{1}{2}\int_0^{\delta_e}\frac{\partial U^2}{\partial y}\left(\int_0^y \frac{\partial U}{\partial x}\,\mathrm{d}y'\right)\mathrm{d}y \\ &= -\int_0^{\delta_e} U^2\,\frac{\partial U}{\partial x}\,\mathrm{d}y + \frac{1}{2}\int_0^{\delta_e}\frac{\partial}{\partial y}\left(U^2\int_0^y \frac{\partial U}{\partial x}\,\mathrm{d}y'\right)\mathrm{d}y - \frac{1}{2}\int_0^{\delta_e} U^2\,\frac{\partial U}{\partial x}\,\mathrm{d}y \\ &= -\frac{1}{2}\int_0^{\delta_e}\frac{\partial U^3}{\partial x}\,\mathrm{d}y + \frac{1}{2}\,U_e^2\int_0^{\delta_e}\frac{\partial U}{\partial x}\,\mathrm{d}y \\ &= -\frac{1}{2}\,\frac{\mathrm{d}}{\mathrm{d}x}\int_0^{\delta_e} U^3\,\mathrm{d}y + \frac{1}{2}\,U_e^2\,\frac{\mathrm{d}}{\mathrm{d}x}\int_0^{\delta_e} U\,\mathrm{d}y \\ &= -\frac{1}{2}\,\frac{\mathrm{d}}{\mathrm{d}x}(U_e^3(\delta_e-\delta_1-\delta_3)) + \frac{1}{2}\,U_e^2\,\frac{\mathrm{d}}{\mathrm{d}x}(U_e(\delta_e-\delta_1)) \\ &= \frac{1}{2}\,\frac{\mathrm{d}(U_e^3\delta_3)}{\mathrm{d}x} - U_e\,\frac{\mathrm{d}U_e}{\mathrm{d}x}\int_0^{\delta_e} U\,\mathrm{d}y.\end{aligned} \tag{B3}$$

Note that the integration by parts rule was applied to the second integral on the first line. Figure 15(*a*) illustrates the two components on the right-hand side of (B3). Under a weak pressure gradient, the second component is nearly zero and smaller than the first component. However, under a strong pressure gradient, the magnitude of the second component becomes significantly larger, exceeding that of the first component more than tenfold.

It can be shown that the second component on the right-hand side of (B3) is closely related to the pressure gradient and wall-normal flow in the TBL. Recently, Wei *et al.* (2023*a*) derived an analytical equation for $V_e$ in TBL flows under pressure gradient as follows:

$$V_e = -\delta_e\,\frac{\mathrm{d}U_e}{\mathrm{d}x} + \frac{\mathrm{d}(U_e\delta_1)}{\mathrm{d}x}. \tag{B4}$$

Hence the second component on the right-hand side of (B3) can be expressed as

$$-U_e\,\frac{\mathrm{d}U_e}{\mathrm{d}x}\int_0^{\delta_e} U\,\mathrm{d}y = -U_e^2\,\frac{\mathrm{d}U_e}{\mathrm{d}x}\,(\delta_e-\delta_1) = U_e^2\left(V_e - U_e\,\frac{\mathrm{d}\delta_1}{\mathrm{d}x}\right). \tag{B5}$$

Note that $U_e\,\mathrm{d}\delta_1/\mathrm{d}x$ represents the mean wall-normal velocity at the boundary layer edge in the ZPG TBL (see Wei *et al.* 2023*b*).

The variation of $V_e$ and $U_e\,\mathrm{d}\delta_1/\mathrm{d}x$ in the DNS data of Coleman *et al.* (2018) is presented in figure 15(*b*). Under weak pressure gradients, near the inlet and outlet of the simulation domain, figure 15(*b*) shows that $V_e$ closely approximates $U_e\,\mathrm{d}\delta_1/\mathrm{d}x$. However, under a



https://doi.org/10.1017/jfm.2024.1195 Published online by Cambridge University Press

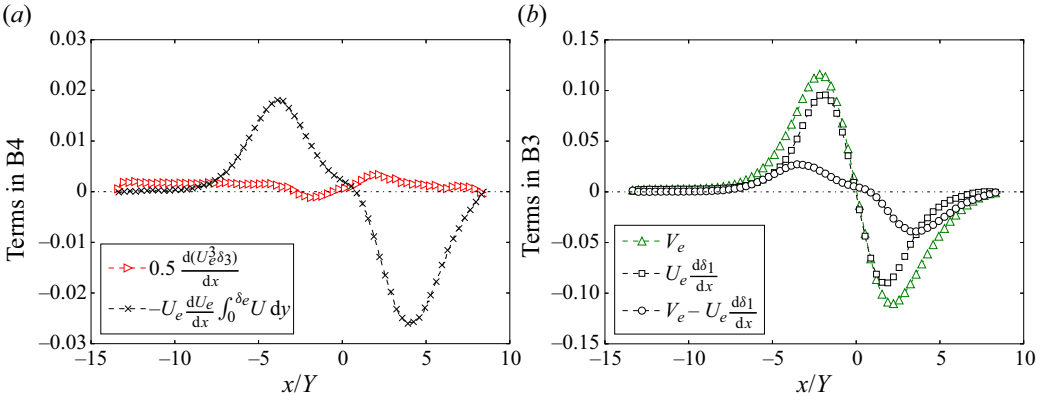



Figure 15. (*a*) Two components on the right-hand side of (B3). (*b*) Plots of $V_e$ and $U_e\,\mathrm{d}\delta_1/\mathrm{d}x$. Data are from DNS of Coleman *et al.* (2018).

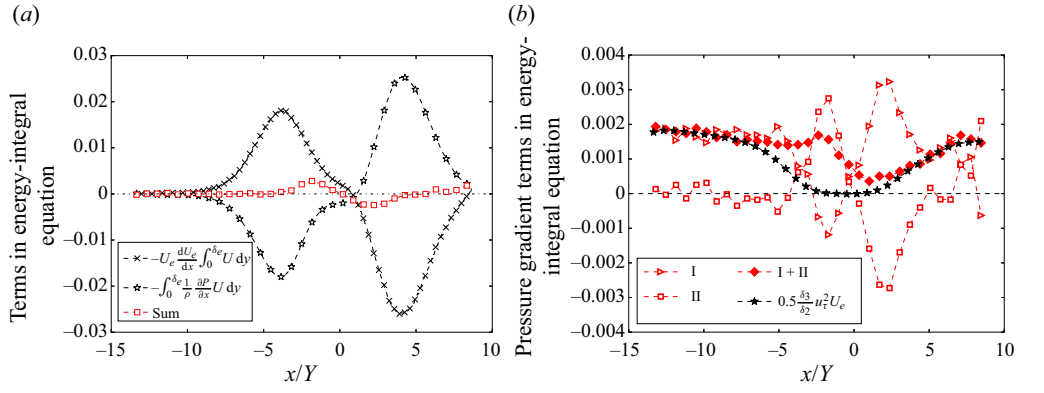



Figure 16. (*a*) Variation of $-U_e\,(\mathrm{d}U_e/\mathrm{d}x)\int_0^{\delta_e} U\,\mathrm{d}y$, $-\int_0^{\delta_e}(1/\rho)(\partial P/\partial x)U\,\mathrm{d}y$, and sum. (*b*) Terms I, II and sum, compared with the ZPG approximation equation. Data are from DNS of Coleman *et al.* (2018).

strong APG, $V_e$ surpasses $U_e\,\mathrm{d}\delta_1/\mathrm{d}x$. Similarly, under a strong FPG, the magnitude of $V_e$ also exceeds that of $U_e\,\mathrm{d}\delta_1/\mathrm{d}x$.

Many previous studies have assumed that $\partial(P/\rho)/\partial x \approx -U_e\,\mathrm{d}U_e/\mathrm{d}x$. However, Wei *et al.* (2024) have shown that this assumption is valid only for weak pressure gradients, becoming invalid under strong pressure gradients. Figure 16(*a*) illustrates the second component on the right-hand side of (B3) and the integral resulting from the pressure force multiplied by $U$. The figure indicates that both components are close to zero under weak pressure gradients. However, under strong pressure gradients, they differ, yet their sum is significantly smaller than either component alone. Moreover, the magnitude of the sum is comparable to terms I, III, IV, V, VI in (3.2). Therefore, the second component on the right-hand side of (B3) is combined with the integral arising from the pressure gradient to form term II in (3.2).

Figure 16(*b*) presents the terms I, II, and their sum. Additionally, the approximation given by (2.3) is also included, demonstrating that the approximation equation aligns well with the sum of terms I and II in the region where the pressure gradients are small.



https://doi.org/10.1017/jfm.2024.1195 Published online by Cambridge University Press

## References


ABE, H. & ANTONIA, R.A. 2016 Relationship between the energy dissipation function and the skin friction law in a turbulent channel flow. *J. Fluid Mech.* **798**, 140–164.

AFZAL, N. 1982 Fully developed turbulent flow in a pipe: an intermediate layer. *Arch. Appl. Mech.* **52** (6), 355–377.

BAIDYA, R., PHILIP, J., HUTCHINS, N., MONTY, J.P. & MARUSIC, I. 2017 Distance-from-the-wall scaling of turbulent motions in wall-bounded flows. *Phys. Fluids* **29** (2), 020712.

BAIDYA, R., PHILIP, J., HUTCHINS, N., MONTY, J.P. & MARUSIC, I. 2021 Spanwise velocity statistics in high-Reynolds-number turbulent boundary layers. *J. Fluid Mech.* **913**, A35.

BRADSHAW, P. 1965 The response of a retarded equilibrium turbulent boundary layer to the sudden removal of pressure gradient. *Tech. Rep.* NPL Aero. Rep. 1145.

BRADSHAW, P. 1966 The turbulence structure of equilibrium boundary layers. *Tech. Rep.* NPL Aero. Rep. 1184.

CASTILLO, L., WANG, X. & GEORGE, W.K. 2004 Separation criterion for turbulent boundary layers via similarity analysis. *Trans. ASME J. Fluids Engng* **126** (3), 297–304.

CLAUSER, F.H. 1954 Turbulent boundary layers in adverse pressure gradients. *J. Aeronaut. Sci.* **21**, 91–108.

CLAUSER, F.H. 1956 The turbulent boundary layer. *Adv. Appl. Mech.* **4**, 1–51.

COLEMAN, G.N., RUMSEY, C.L. & SPALART, P.R. 2018 Numerical study of turbulent separation bubbles with varying pressure gradient and Reynolds number. *J. Fluid Mech.* **847**, 28–70.

COLES, D.E. & HIRST, E.A. 1969 *Computation of Turbulent Boundary Layers – 1968 AFOSR-IFP-Stanford Conference. Vol. 2: Compiled Data*. Stanford University.

GRIFFIN, K.P., FU, L. & MOIN, P. 2021 General method for determining the boundary layer thickness in nonequilibrium flows. *Phys. Rev. Fluids* **6** (2), 024608.

GUNGOR, A.G., MACIEL, Y., SIMENS, M.P. & SORIA, J. 2016 Scaling and statistics of large-defect adverse pressure gradient turbulent boundary layers. *Intl J. Heat Fluid Flow* **59**, 109–124.

GUNGOR, T.R., GUNGOR, A.G. & MACIEL, Y. 2024 Turbulent boundary layer response to uniform changes of the pressure force contribution. *J. Fluid Mech.* **997**, A75.

GUNGOR, T.R., MACIEL, Y. & GUNGOR, A.G. 2022 Energy transfer mechanisms in adverse pressure gradient turbulent boundary layers: production and inter-component redistribution. *J. Fluid Mech.* **948**, A5.

VON KÁRMÁN, T. 1921 Über laminare und turbulente reibung. *Z. Angew. Math. Mech.* **1** (4), 233–252.

VON KÁRMÁN, T. 1934 Turbulence and skin friction. *J. Aeronaut. Sci.* **1** (1), 1–20.

LAADHARI, F. 2007 Reynolds number effect on the dissipation function in wall-bounded flows. *Phys. Fluids* **19** (3), 038101.

LUDWIEG, H. & TILLMANN, W. 1949 Untersuchungen über die Wandschubspannung in turbulenten Reibungsschichten. *Ing.-Arch.* **17**, 288–299.

MACIEL, Y., WEI, T., GUNGOR, A.G. & SIMENS, M.P. 2018 Outer scales and parameters of adverse-pressure-gradient turbulent boundary layers. *J. Fluid Mech.* **844**, 5–35.

MANHART, M. & FRIEDRICH, R. 2002 DNS of a turbulent boundary layer with separation. *Intl J. Heat Fluid Flow* **23** (5), 572–581.

MONIN, A.S. & YAGLOM, A.M. 1965 *Statistical Fluid Mechanics, Volume I: Mechanics of Turbulence*. MIT Press.

PERRY, A.E. & SCHOFIELD, W.H. 1973 Mean velocity and shear stress distributions in turbulent boundary layers. *Phys. Fluids* **16** (12), 2068–2074.

POHLHAUSEN, K. 1921 Zur näherungsweisen integration der differentialgleichung der iaminaren grenzschicht. *Z. Angew. Math. Mech.* **1** (4), 252–290.

RENARD, N. & DECK, S. 2016 A theoretical decomposition of mean skin friction generation into physical phenomena across the boundary layer. *J. Fluid Mech.* **790**, 339–367.

ROTTA, J. 1953 On the theory of the turbulent boundary layer. *NACA Tech. Mem.* 1344. NACA.

ROTTA, J. 1962 Turbulent boundary layers in incompressible flow. *Prog. Aerosp. Sci.* **2** (1), 1–95.

SCHLATTER, P. & ÖRLÜ, R. 2010 Assessment of direct numerical simulation data of turbulent boundary layers. *J. Fluid Mech.* **659**, 116–126.

SCHLICHTING, H. 1979 *Boundary-Layer Theory*. McGraw-Hill.

SCHUBAUER, G.B. & KLEBANOFF, P.S. 1950 Investigation of separation of the turbulent boundary layer. *NASA Tech. Rep.* TN 2133. NASA.

SCHUBAUER, G.B. & KLEBANOFF, P.S. 1951 Investigation of separation of the turbulent boundary layer. *NACA Tech. Rep.* TR-1030. NACA.

SCHUBAUER, G.B. & SPRANGENBERG, W.G. 1960 Forced mixing in boundary layers. *J. Fluid Mech.* **8**, 10–32.




https://doi.org/10.1017/jfm.2024.1195 Published online by Cambridge University Press

SENTHIL, S., KITSIOS, V., SEKIMOTO, A., ATKINSON, C. & SORIA, J. 2020 Analysis of the factors contributing to the skin friction coefficient in adverse pressure gradient turbulent boundary layers and their variation with the pressure gradient. *Intl J. Heat Fluid Flow* **82**, 108531.

SIMPSON, R.L. 1989 Turbulent boundary-layer separation. *Annu. Rev. Fluid Mech.* **21** (1), 205–232.

SKÅRE, P.E. & KROGSTAD, P.A. 1994 A turbulent equilibrium boundary layer near separation. *J. Fluid Mech.* **272**, 319–348.

SREENIVASAN, K.R. & SAHAY, A. 1997 The persistence of viscous effects in the overlap region, and the mean velocity in turbulent pipe and channel flows. arXiv:9708016.

STRATFORD, B.S. 1959 The prediction of separation of the turbulent boundary layer. *J. Fluid Mech.* **5** (1), 1–16.

TENNEKES, H. & LUMLEY, J.L. 1972 *A First Course in Turbulence*. MIT Press.

WEI, T. 2018 Integral properties of turbulent-kinetic-energy production and dissipation in turbulent wall-bounded flows. *J. Fluid Mech.* **854**, 449–473.

WEI, T., FIFE, P., KLEWICKI, J. & MCMURTRY, P. 2005 Properties of the mean momentum balance in turbulent boundary layer, pipe and channel flows. *J. Fluid Mech.* **522**, 303–327.

WEI, T. & KLEWICKI, J. 2016 Scaling properties of the mean wall-normal velocity in zero-pressure-gradient boundary layers. *Phys. Rev. Fluids* **1** (8), 082401.

WEI, T. & KLEWICKI, J. 2023 Integral relation in zero-pressure-gradient boundary layer flows. *Phys. Rev. Fluids* **8**, 124601.

WEI, T. & KNOPP, T. 2023 Outer scaling of the mean momentum equation for turbulent boundary layers under adverse pressure gradient. *J. Fluid Mech.* **958**, A9.

WEI, T., LI, Z., KNOPP, T. & VINUESA, R. 2023*a* The mean wall-normal velocity in turbulent-boundary-layer flows under pressure gradient. *J. Fluid Mech.* **975**, A27.

WEI, T., LI, Z. & WANG, Y. 2023*b* New formulations for the mean wall-normal velocity and Reynolds shear stress in turbulent boundary layer under zero pressure gradient. *J. Fluid Mech.* **969**, A3.

WEI, T., LI, Z. & WANG, Y. 2024 New momentum integral equation applicable to boundary layer flows under arbitrary pressure gradients. *J. Fluid Mech.* **984**, A64.

WIEGHARDT, K. 1945 Turbulente grenzschichten. *Tech. Rep*.

WIEGHARDT, K. 1948 Über einen energiesatz zur berechnung laminarer grenzschichten. *Ing.-Arch.* **16** (3), 231–242.

https://doi.org/10.1017/jfm.2024.1195 Published online by Cambridge University Press